# Duality of Topological Defects in Hexagonal Manganites

Fei-Ting Huang,[1] Xueyun Wang,[1] Sinead M. Griffin,[2] Yu Kumagai,[2] Oliver Gindele,[2] Ming-Wen Chu,[3] Yoichi Horibe,[1] Nicola A. Spaldin,[2] and Sang-Wook Cheong[1,*]

[1]*Rutgers Center for Emergent Materials and Department of Physics and Astronomy, Rutgers University, Piscataway, New Jersey 08854, USA*

[2]*Materials Theory, ETH Zurich, Wolfgang-Pauli-Strasse 27, 8093 Zürich, Switzerland*

[3]*Center for Condensed Matter Sciences, National Taiwan University, Taipei 106, Taiwan*

(Received 24 June 2014; published 30 December 2014)

We show that the spontaneous symmetry breaking in multiferroic hexagonal manganites can be chemically manipulated to yield two complementary ground states: the well-known ferroelectric $P6_3cm$ and an antipolar $P\bar{3}c$ phase. Both symmetry breakings yield topologically protected vortex defects, with the antipolar vortices dual to those of the ferroelectric. This duality stems from the existence of 12 possible angles of $MnO_5$ tilting, and broad strain-free walls with low energy spontaneously emerge through an intermediate $P3c1$ state, providing a complete unified symmetry description.

DOI: 10.1103/PhysRevLett.113.267602 PACS numbers: 77.80.Dj, 61.72.-y, 68.37.Ma, 75.60.Ch

The hexagonal rare-earth manganites ($h$-$R$MnO$_3$, $R$ = Sc, Y, Ho-Lu) [1–5] with their combined and coupled structural distortions [1,6,7], ferroelectricity [3,8], magnetism [9,10], and electronic conduction [11,12] provide an interesting paradigm in the quest for novel multifunctional materials. The structural phase transition underlying their unusual behaviors is now understood to be described by a Mexican hat-type potential [2] in which the primary order parameter is a $K_3$ mode characterized by trimerizing tilts of the $MnO_5$ trigonal bipyramids [2,3,8]. For large $K_3$ amplitudes the energy is reduced to six stable states through an angle-dependent coupling to a secondary polar $\Gamma_2^-$ mode consisting of a polar displacement of the $R$-cation sublattice. For positive $\Gamma_2^-$ the coupling is most energy lowering for $K_3$ tilt angles of 0°, 120°, and 240°, whereas negative $\Gamma_2^-$ favors angles of 60°, 180°, and 300° [Fig. 1(a) blue arrows and Supplemental Material, Figs. S1(a)–1(b) [13]], yielding a modified Mexican hat potential with six minima in the brim that correspond to alternating polarization directions. A consequence of this unusual potential landscape is the striking cloverleaf domain structure in the ferroelectric (FE) $P6_3cm$ phase, with topologically protected $Z_2 \times Z_3$ FE vortices at the meeting point of six domains with opposite electric polarization (+, −) interlocked with three structural antiphases ($\alpha, \beta, \gamma$) [5,6,14–17]. Additionally, the zero-polarization primary order parameter enables formation of electrostatically unfavorable head-to-head and tail-to-tail ferroelectric domain walls (DWs), which exhibit high conductivity because of the large charge carrier densities that accumulate to screen their polar discontinuities [11,12].

Recently, $h$-InMnO$_3$ has been shown to exist in the same FE structure as the $h$-$R$MnO$_3$ materials, with a similar $Z_2 \times Z_3$ domain structure [Fig. 1(b)] [18]. Hexagonal InMnO$_3$ is of additional interest, however, because an almost degenerate [19], partially undistorted antipolar (PUA) phase with $P\bar{3}c$ symmetry can be stabilized through fast quenching [18,19]. This PUA phase has never been found in the $h$-RMnO$_3$ series, where it is of substantially higher energy [20]. The $P\bar{3}c$ structure is obtained from the high-temperature $P6_3/mmc$ prototype by tilting of the $MnO_5$ bipyramids at intermediate angles ($n$ odd) of 30°, 90°, 150°, 210°, 270°, and 330°, accompanied by an up-down-no pattern of In-ion displacements. From symmetry arguments, this PUA state should, in principle, present $Z_2 \times Z_3$ PUA vortices analogous to those in the FE

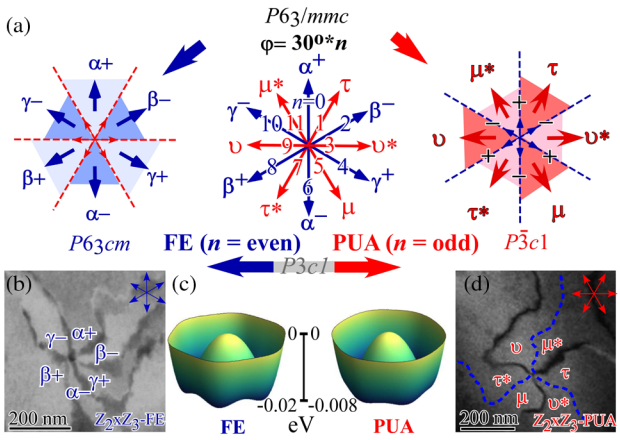


FIG. 1 (color online). (a) Twelve possible angles of $MnO_5$ tilting and relevant phases. Schematics of FE (left) and PUA (right) vortices. (b) A superlattice DF-TEM image showing a FE vortex in $h$-InMnO$_3$. (c) Calculated Mexican hat-shape energy landscapes for FE (left) and PUA (right) $h$-InMnO$_3$. Note the presence of six minima in the brim and the phase shift of 30° between them. (d) A superlattice DF-TEM image showing three obvious DWs meeting at one point (PUA vortex) in $h$-In(Mn, Ga)O$_3$. The blue dashed lines depict the three hidden walls.

 

structure, with six possible domains corresponding to three different phase shifts ($\tau$, $\upsilon$, $\mu$) combined with two oxygen-distortion handedness [Fig. 1(a) $n$ = odd; $\tau$, $\upsilon^*$, $\mu$, $\tau^*$, $\upsilon$, $\mu^*$ and structures in Supplemental Material, Figs. S1(c)–1(d) [13]]. Such $Z_2 \times Z_3$ PUA vortices were not previously observed in quenched $h$-$InMnO_3$, however, probably because of high structural disorder in the quenched specimens [18]. Here, we show the existence of these $Z_2 \times Z_3$ PUA vortices, and show that they are "dual" to the well-known $Z_2 \times Z_3$ FE vortices in their exchange of ferroelectricity and antipolarity.

Here we adopt an alternative approach to achieving PUA $InMnO_3$: Using Ga doping on the Mn site we apply an effective in-plane compressive strain which was shown previously to tip the energy balance between the FE and PUA phases so that PUA is the ground state [19]. High-quality polycrystalline $In(Mn_{1-x}Ga_x)O_3$ ($0 \le x \le 1$) samples were prepared using a solid-state reaction method (the details are given in Supplemental Material [13]). Our measured lattice parameters, obtained using powder x-ray diffraction, as a function of Ga concentration are shown in Supplemental Material, Fig. S2 [13]. The atomic configurations within the domains and DWs were determined and explained using scanning transmission electron microscopy (STEM, JEOL-2100F microscope equipped with a spherical aberration Cs corrector), first-principles calculation of the energy landscape, and symmetry analysis. Full experimental and computational details [21–24] are given in the Supplemental Material [13].

We begin by discussing the FE phase of $h$-$InMnO_3$. First, we calculate the energy landscape using density functional theory to extract the coefficients in the energy expansion

$$F = \frac{a}{2}Q^2 + \frac{b}{4}Q^4 + \frac{Q^6}{6}(c + d\cos 6\phi) - gQ^3P\cos 3\phi + \frac{g'}{2}Q^2P^2 + \frac{f}{2}P^2, \quad (1)$$

which is derived in detail in Refs. [2,8]. Here, $Q$ and $\phi$ are the magnitude and phase, respectively, of the trimerizing $K_3$ mode, and $P$ is the magnitude of the polar $\Gamma_2^-$ mode. We stabilize the FE phase computationally by using the generalized gradient approximation (GGA) plus Hubbard correction (GGA + $U$) method [19,20]; other details of the *ab initio* calculations are given in the Supplemental Material, Table S1 [13]. Our calculated potential energy landscape is shown in Fig. 1(c) (left).

We see that the energy surface has a similar Mexican hat form as found previously for $YMnO_3$ [2]. As expected, there are six minima in the brim of the hat at $30°^*n$ ($n$ even), corresponding to the six FE ground states. In contrast to the case of the robustly FE $YMnO_3$, where the barriers between the minima are 25 meV, in this case the barriers between the minima are only around 4 meV. The maxima of these small energy barriers lie as expected at the intermediate tilt angles of $30°^*n$ ($n$ odd) corresponding to the almost-degenerate PUA phase. Indeed, because of its intermediate nature, the PUA phase was suggested previously as a possible candidate for the DW structure in the FE $h$-$RMnO_3$ compounds [6]. Such DWs (type-I) have been observed in $TmMnO_3$ and $LuMnO_3$ using HAADF imaging although only at the surface of samples [25], and were shown using first-principles calculations to be higher energy than an abrupt DW with a discontinuous jump from one domain structure to the next (type-II) [20]. In the case of FE $h$-$InMnO_3$, however, the small energy barriers suggest that DWs of PUA structure should be energetically favorable.

Indeed, we find this to be the case. In Figs. 2(a)–2(b), we show our measured HAADF-STEM images of the two types of DWs that we find commonly in FE $h$-$InMnO_3$, with the corresponding structural models in Figs. 2(c)–2(d). The type-I wall has a smooth transition from one ferroelectric domain to another via a layer of the intermediate PUA structure; the type-II wall, in contrast, exhibits an abrupt transition between domains of opposite polarization. In contrast to the case of $YMnO_3$, the type (I) walls are common in FE $h$-$InMnO_3$, and, in fact, we find that the two wall types tend to alternate around each vortex core.

Next we turn our attention to the PUA $P\bar{3}c$ phase. As mentioned above, we stabilize the $P\bar{3}c$ phase experimentally by doping with Ga on the Mn site (see details in the Supplemental Material, Sec. 2 [13]). The smaller-sized Ga versus Mn ions—the Shannon radii in five coordination are 0.55 and 0.58 Å, respectively—combined with the

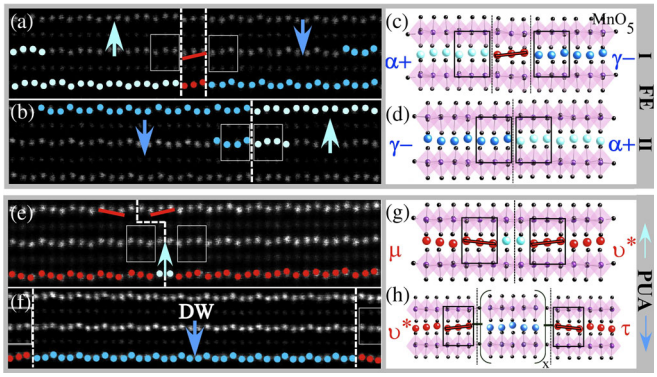


FIG. 2. (color online). (a-b) HAADF images of the two types of DWs in FE $h$-$InMnO_3$. Some In ions are superimposed with blue and light blue spheres to indicate oppositely polarized regions, or with red spheres to indicate the PUA region. (c)–(d) Schematic models of the two types of DWs. Mn and O ions are shown with pink and black spheres, respectively. White dashed lines indicate DWs. (e)–(f) HAADF images of the two distinct wall types in PUA $h$-$In(Mn, Ga)O_3$. Again, some In ions have colored spheres superimposed. The rectangles and red lines indicate up-no-down and down-no-up PUA units. (e) A narrow DW with upward In distortions, and (f) a broad DW with downward net In displacements. (g)–(h) Schematic models of the two types of DWs.

presence of out-of-plane Ga $d$ orbitals, produces a compressive in-plane strain (Fig. S2 [13]), which stabilizes the PUA phase for Ga concentrations up to 40%. Above this value we obtain the high-symmetry reference $P6_3/mmc$ phase of $InGaO_3$ [26].

Computationally, we stabilize the PUA phase by using the Perdew-Burke-Ernzerhof–GGA [19,20], then again extract the coefficients in the free energy [Eq. (1)]. The calculated potential energy landscape is shown in Fig. 1(c) (right). Again, the energy landscape has a Mexican hat form with quasi-$U(1)$ symmetry at its peak and six minima in the brim. An important difference with the FE case, however, is that here the minima are at angles of $30°*n$, with $n$ odd, exactly intermediate between those of the FE case. Another striking difference is the depth of the minima, which here are barely visible, with barriers between them of only 1 meV, so that the symmetry remains close to $U(1)$ even in the brim of the hat. To understand the implications of the small energy barriers on the domain structure, we calculated the properties of a DW, again using the Perdew-Burke-Ernzerhof–GGA functional to ensure the PUA ground state (see Supplemental Material [13]). Our calculated DW structure is shown in Fig. 3(a). We obtain a wide DW, with a gradual evolution of the tilt angle from −30° to 30° and a corresponding evolution of the In displacement amplitudes. The calculated wall energy is very low (4.6 $mJ/m^2$). The net displacement of the In sublattice has the same orientation throughout the wall leading to a polarization which reaches its maximum value at the middle of the wall, where the tilt angle becomes 0° corresponding to the $\alpha^+$ ferroelectric phase [Fig. 3(a)].

Figures 1(d) and 3(b) show our superlattice DF-TEM images of PUA domains in $h$-$InMn_{0.95}Ga_{0.05}O_3$. At first sight, Fig. 3(b) appears to show a $Z_3$ pattern, with three lines meeting at one point, which would contradict the known $P\bar{3}c$ symmetry. Careful examination by tilting to tune contrast through enhancing excitation error reveals, however, six domains, as shown in Figs. 3(c)–3(d), with "hidden" walls alternating with easily visible walls. Our DF-TEM images for the first time demonstrate a $Z_2 \times Z_3$ PUA vortex pattern in $h$-$In(Mn, Ga)O_3$ comparable with that in the FE $h$-$RMnO_3$ (see vortex models in Supplemental Material, Fig. S3 [13]), although, in this case, three of the DWs are clearly of a different nature than the other three. Since strain provides the main diffraction contrast change in our DF-TEM images, we associate the weak-contrast walls with a lower internal strain field (see Supplemental Material, Sec. 4 [13]).

Our HAADF-STEM data shown in Figs. 2(e)–2(f) with structural models in Figs. 2(g)–2(h) indicate the origin of the two wall types: two wall types of alternating polarization around each vortex, with one set broad (and hence having a low strain field), and one set narrow (with correspondingly higher strain). Defining the "up-no-down" and "down-no-up" repeat units marked by rectangles in Fig. 2(g) as belonging to neighboring phases $\mu$ and $\upsilon^*$,

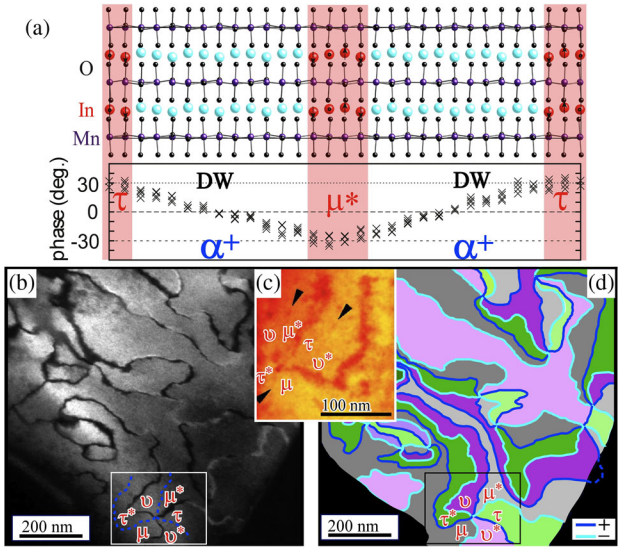


FIG. 3 (color online). (a) Calculated DW structure between two PUA regions. The red regions correspond to the $\mu^*$ (−30°) and $\tau$ (+30°) phases, respectively. We find a broad wall with a gradual evolution of the In displacements (upper panel) and phase angles of the $MnO_5$ bipyramids (lower panel). (b) DF-TEM image of $h$-$InMn_{0.95}Ga_{0.05}O_3$ and (c) black arrows indicate the three hidden walls with weaker contrasts emerging from the vortex core, revealed in DF-TEM images at large excitation error condition. (d) The mapping of polarized DWs in the PUA phase, corresponding to (b).

respectively, we see that one wall in Fig. 2(e) transitions sharply from $\mu$ to $\upsilon^*$ with a $\mu$-up-up-$\upsilon^*$ In displacement pattern. Such narrow DWs show strong diffraction contrast in the DF-TEM image [Fig. 3(c)]. The other wall in Fig. 2(f) is of opposite polarity, with a "down-down" In distortion at its center, and is much broader with a $\upsilon^*$ … -down-down- … $\tau$ pattern, where the "…" indicate units that are intermediate between the $\upsilon^*$ and $\tau$ structures, with gradually increasing (in the down direction) then decreasing In distortion amplitudes. These broad DWs match those of our DFT wall calculations shown in Fig. 3(a) and are responsible for the weak-contrast boundary found in Fig. 3(c), and Fig. S4a of [13]. Note that these two DWs, which have opposite polarity and a significant difference in wall width, always alternate around a vortex core as shown in Fig 3(d). Note also that there is no single preferred polarization direction of broad walls throughout the sample, with different regions having up- or down-polarization broad walls, consistent with the overall symmetry (see Supplemental Materials Sec. 5 [13]).

Finally, we quantify the evolution of the In displacements across a broad wall, using HAADF-STEM. Figures 4(a)–4(b) show a $10 \times 10$ nm HAADF-STEM image of a broad DW in PUA $h$-$In(Mn_{0.95}Ga_{0.05})O_3$ and the corresponding mapping of In displacements. The viewing direction is along the crystallographic [010] direction (indexed to the $P6_3cm$ structure). The insets in

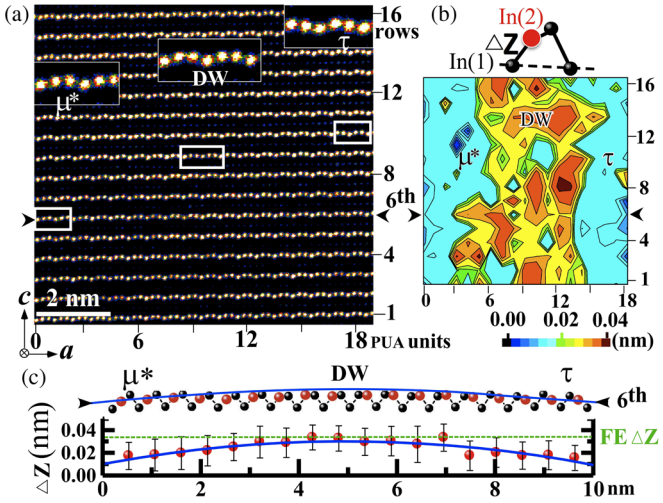


FIG. 4 (color online). (a) HAADF image showing an up-polarized broad DW viewed along [010]. The left and right rectangular insets ($\mu^*$ and $\tau$) show magnified regions with phases different by 60°, and the central inset shows the magnified DW region. (b) Two-dimensional $\Delta Z$ mapping from (a). The Wyckoff position of In(1) is $4d$ $(1/3, 2/3, z)$ and of In(2) is $2b$ (0, 0, 0). (c) In-ion displacement (upper panel) extracted from the sixth In row and the corresponding $\Delta Z$ profile (lower panel). Blue broken line in the top panel is a guide to show the In(2) site (red spheres) evolution. The experimental $\Delta Z$ value of FE $h$-$InMnO_3$ is marked in a green dashed line for comparison.

the left and right side of Fig. 4(a) show magnifications overlying the respective rectangular areas which we find to be related by a phase shift of 60°; we label them $\mu^*$ and $\tau$, respectively. We define $\Delta Z$, the difference in $z$ coordinate between two symmetry-inequivalent In sites, as a measure of the amplitude of the In displacements (see Supplemental Material, Sec. 6 [13]). We obtain an average wall width ~5 nm, determined from the magnitude of the In(2) displacement. The broad DWs range from 5–12 unit cells (25–61 Å) wide in different regions, consistent with our DFT calculations, and in contrast to the narrow DWs in FE $h$-$InMnO_3$. In Fig. 4(c), the $\Delta Z$ profile along the sixth In row of Figs. 4(a)–4(b) shows that, as expected, the In-ion shift achieves its maximum value of ~0.035 nm close to the wall center; for comparison, the experimental value in FE $h$-$InMnO_3$ is $0.034 \pm 0.003$ nm (see Supplemental Material, Sec. 6 [13]). By comparison with Fig. 3(a), we associate our measured gradual evolution of the In positions across the boundary shown in Fig. 4 with a corresponding gradual change in the tilting angle of the $MnO_5$ bipyramids.

By symmetry, condensation of the $K_3$ mode from the high-symmetry $P6_3/mmc$ phase allows three possible space groups: $P\bar{3}c$, $P6_3cm$, and $P3c1$. $P6_3cm$ and $P\bar{3}c$ are direct subgroups of $P6_3/mmc$, and as already discussed manifest in the FE ($\phi = 30°{}^*n$ with $n$ even) and PUA ($\phi = 30°{}^*n$ with $n$ odd) structures [Fig. 1(a)]. The $P3c1$ structure must have a phase which is a noninteger multiple of 30°, corresponding to an arbitrary $MnO_5$-bipyramid tilting angle. This is indeed the case for the broad wall regions in Fig. 4, which we therefore assign to the $P3c1$ space group. We note that since $P3c1$ is a subgroup of both $P\bar{3}c$ and $P6_3cm$, it is expected by symmetry to link the FE and PUA phases. It has never been observed in the $h$-$RMnO_3$ series because of the higher energy barriers between the FE domains and the resulting narrow DWs in those systems. Note that such crystallographic connection between two competing phases via an intermediate symmetry state has been found in the superconducting $La_{2-x}B_xCuO_4$ system ($B$ = Ba, Sr) [27] and at the so-called morphotropic phase boundaries (MPB) of ferroelectric $PbZr_{1-x}Ti_xO_3$ [28]. However, the low DW energy associated with the unusual duality that we present here leads to broad DWs, distinct from prototypical ferroelastics and ferroelectrics which have sharp walls with large strain gradients [6,20,29–33] (Supplemental Material, Sec. 7 and Table S2 [13]). Other relevant comparisons for our polar domain walls separating nonpolar domains are the polar behaviors reported at ferroelastic twin boundaries in paraelectric $CaTiO_3$ [34] and at translational antiphase boundaries in antiferroelectric $PbZrO_3$ [35].

In summary, we report, for the first time, the stabilization of the antipolar PUA phase in $h$-$InMnO_3$ with a slight Ga doping, and the existence of new antipolar PUA vortex domains. In addition, we discover a unique duality between topological PUA and FE vortices. We show that the characters of the DWs differ, with narrow antipolar walls forming in the FE phase, and broad (up to 6 nm) polar walls in the PUA phase. The broad DWs in the PUA phase exhibit progressive evolutions of In displacements and polyhedral tilt angles, corresponding to the expected $P3c1$ intermediate symmetry that we identify for the first time. Our discoveries unveil unprecedented interrelationships among topological defect duality, lattice symmetry and energetics, suggesting future studies of practical applications of topological defects.

We thank S. Mori (Osaka Prefecture University) and K. Kurushima (Toray Research Center) for help with the STEM experiments. We would also like to acknowledge Pierre Toledano for useful discussions. The work at Rutgers is funded by the Gordon and Betty Moore Foundation's EPiQS Initiative through Grant No. GBMF4413 to the Rutgers Center for Emergent Materials, and that at ETH by the ERC Advanced Grant program, No. 291151, by the ETH Zurich, and by the JSPS Postdoctoral Fellowships for Research Abroad (Y.K.).

*sangc@physics.rutgers.edu

[1] T. Katsufuji, M. Masaki, A. Machida, M. Moritomo, K. Kato, E. Nishibori, M. Takata, M. Sakata, K. Ohoyama, K. Kitazawa, and H. Takagi, Phys. Rev. B **66**, 134434 (2002).

[2] S. Artyukhin, K. T. Delaney, N. A. Spaldin, and M. Mostovoy, Nat. Mater. **13**, 42 (2013).
[3] B. B. Van Aken, T. T. M. Palstra, A. Filippetti, and N. A. Spaldin, Nat. Mater. **3**, 164 (2004).
[4] S.-W. Cheong and M. Mostovoy, Nat. Mater. **6**, 13 (2007).
[5] S. C. Chae, Y. Horibe, D. Y. Jeong, N. Lee, K. Iida, M. Tanimura, and S. W. Cheong, Phys. Rev. Lett. **110**, 167601 (2013).
[6] T. Choi, Y. Horibe, H. T. Yi, Y. J. Choi, W. Wu, and S. W. Cheong, Nat. Mater. **9**, 253 (2010).
[7] S. Lee, A. Pirogov, M. Kang, K.-H. Jang, M. Yonemura, T. Kamiyama, S. W. Cheong, F. Gozzo, N. Shin, H. Kimura, Y. Noda, and J. G. Park, Nature (London) **451**, 805 (2008).
[8] C. J. Fennie and K. M. Rabe, Phys. Rev. B **72**, 100103 (2005).
[9] Y. Geng, N. Lee, Y. J. Choi, S. W. Cheong, and W. Wu, Nano Lett. **12**, 6055 (2012).
[10] Y. Geng, H. Das, A. L. Wysocki, X. Wang, S. W. Cheong, M. Mostovoy, C. J. Fennie, and W. Wu, Nat. Mater. **13**, 163 (2013).
[11] W. Wu, Y. Horibe, N. Lee, S. W. Cheong, and J. R. Guest, Phys. Rev. Lett. **108**, 077203 (2012).
[12] D. Meier, J. Seidel, A. Cano, K. Delaney, Y. Kumagai, M. Mostovoy, N. A. Spaldin, R. Ramesh, and M. Fiebig, Nat. Mater. **11**, 284 (2012).
[13] See Supplemental Material at http://link.aps.org/supplemental/10.1103/PhysRevLett.113.267602 for the details of the experimental method, the domain structures of vortices, *ab* initio parameters, imaging process, and DW-related discussions.
[14] S. C. Chae, N. Lee, Y. Horibe, M. Tanimura, S. Mori, B. Gao, S. Carr, and S. W. Cheong, Phys. Rev. Lett. **108**, 167603 (2012).
[15] S. C. Chae, Y. Horibe, D. Y. Jeong, S. Rodan, N. Lee, and S. W. Cheong, Proc. Natl. Acad. Sci. U.S.A. **107**, 21366 (2010).
[16] M. Mostovoy, Nat. Mater. **9**, 188 (2010).
[17] S. M. Griffin, M. Lilienblum, K. T. Delaney, Y. Kumagai, M. Fiebig, and N. A. Spaldin, Phys. Rev. X **2**, 041022 (2012).
[18] F.-T. Huang, X. Wang, Y. S. Oh, K. Kurushima, S. Mori, Y. Horibe, and S. W. Cheong, Phys. Rev. B **87**, 184109 (2013).
[19] Y. Kumagai, A. A. Belik, M. Lilienblum, N. Leo, M. Fiebig, and N. A. Spaldin, Phys. Rev. B **85**, 174422 (2012).
[20] Y. Kumagai and N. A. Spaldin, Nat. Commun. **4**, 1540 (2013).
[21] G. Kresse and J. Furthmüller, Phys. Rev. B **54**, 11169 (1996).
[22] G. Kresse and D. Joubert, Phys. Rev. B **59**, 1758 (1999).
[23] J. P. Perdew, K. Burke, and M. Ernzerhof, Phys. Rev. Lett. **77**, 3865 (1996).
[24] A. Togo, F. Oba, and I. Tanaka, Phys. Rev. B **78**, 134106 (2008).
[25] Q. H. Zhang, L. J. Wang, X. K. Wei, R. C. Yu, L. Gu, A. Hirata, M. W. Chen, C. Q. Jin, Y. Yao, Y. G. Wang, and X. F. Duan, Phys. Rev. B **85**, 020102 (2012).
[26] D. A. Rusakov, A. A. Belik, S. Kamba, M. Savinov, D. Nuzhnyy, T. Kolodiazhnyi, K. Yamaura, E. Takayama-Muromachi, F. Borodavka, and J. Kroupa, Inorg. Chem. **50**, 3559 (2011).
[27] C. H. Chen, S. W. Cheong, D. J. Werder, and H. Takagi, Physica (Amsterdam) **206C**, 183 (1993).
[28] B. Noheda, D. E. Cox, G. Shirane, R. Guo, B. Jones, and L. E. Cross, Phys. Rev. B **63**, 014103 (2000).
[29] B. Meyer and D. Vanderbilt, Phys. Rev. B **65**, 104111 (2002).
[30] G. Catalan, J. Seidel, R. Ramesh, and J. F. Scott, Rev. Mod. Phys. **84**, 119 (2012).
[31] Y. Wang, C. Nelson, A. Melville, B. Winchester, S. Shang, Z.-K. Liu, D. G. Schlom, X. Pan, and L.-Q. Chen, Phys. Rev. Lett. **110**, 267601 (2013).
[32] J. Padilla, W. Zhong, and D. Vanderbilt, Phys. Rev. B **53**, R5969 (1996).
[33] D. Lee, H. Xu, V. Dierolf, V. Gopalan, and S. R. Phillpot, Appl. Phys. Lett. **98**, 092903 (2011).
[34] S. Van Aert, S. Turner, R. Delville, D. Schryvers, G. Van Tendeloo, and E. K. H. Salje, Adv. Mater. **24**, 523 (2012).
[35] X.-K. Wei, A. K. Tagantsev, A. Kvasov, K. Roleder, C.-L. Jia, and N. Setter, Nat. Commun. **5**, 3031 (2013).